Chemistry–A European Journal
Research Article
doi.org/10.1002/chem.202203432
Chemistry Europe
European Chemical Societies Publishing
www.chemeurj.org

Fabricating Robust Pt Clusters on Sn-Doped CeO_2 for CO Oxidation: A Deep Insight into Support Engineering and Surface Structural Evolution

Qinglong Liu,[a] Peng Yang,[a] Wei Tan,[a] Yu Haowei,[a] Jiawei Ji,[a] Cong Wu,[a] Yandi Cai,[a] Shaohua Xie,[b] Fudong Liu,[b] Song Hong,[c] Kaili Ma,[d] Fei Gao,*[a] and Lin Dong[a]

Abstract: The size effect on nanoparticles, which affects the catalysis performance in a significant way, is crucial. The tuning of oxygen vacancies on metal-oxide support can help reduce the size of the particles in active clusters of Pt, thus improving catalysis performance of the supported catalyst. Herein, Ce–Sn solid solutions (CSO) with abundant oxygen vacancies have been synthesized. Activated by simple CO reduction after loading Pt species, the catalytic CO oxidation performance of Pt/CSO was significantly better than that of Pt/CeO_2. The reasons for the elevated activity were further explored regarding ionic Pt single sites being transformed into active Pt clusters after CO reduction. Due to more exposed oxygen vacancies, much smaller Pt clusters were created on CSO (ca. 1.2 nm) than on CeO_2 (ca. 1.8 nm). Consequently, more exposed active Pt clusters significantly improved the ability to activate oxygen and directly translated to the higher catalytic oxidation performance of activated Pt/CSO catalysts in vehicle emission control applications.

■■Please add academic titles ("Dr." or "Prof.") for the authors in the author line where appropriate■■

Introduction

In response to the increasingly stringent exhaust emission regulations, developing more efficient catalysts for exhaust gas after-treatment systems is an important research priority.[1] Platinum group metals (PGMs), such as Pt, Pd, and Rh, have been widely used as critical active components in emission control catalysts, such as three-way catalysts (TWCs).[2] Among the PGMs, Pt-based catalysts have attracted much attention due to their excellent conclusive activity for carbon monoxide (CO) and hydrocarbons (HCs) oxidation and the low price of Pt relative to Pd and Rh in recent years.[3] Numerous types of research have been carried out to improve the performance of Pt-based catalysts further and reduce the amount of Pt used. To this end, an important route is to increase the number of active sites by reducing the size of Pt species to the nanoscale or atomic scale.[1] Recent studies have shown that particle size is a decisive factor for catalytic performance, especially when the reaction is structure-sensitive, as in the case of CO oxidation on Pt.[4] Pt single-atom catalysts (SACs) with maximum atomic availability recently received considerable attention. A significant challenge is that stable single metal atoms are generally in an oxidized ionic state, which does not correspond to the highest activity state of the catalyst. While after appropriate activation treatment (e.g., steam aging, CO/H_2/HC reduction), the catalytic performance of Pt SACs can be promoted, which should be due to the coordination environment of Pt being drastically altered and ionic Pt SACs being transformed into active Pt clusters.[5] The present studies showed that the oxygen vacancy of the supports played a crucial role in the modulation and activation of the Pt states,[6] i.e., the regulation of surface defects of metal oxides limited the growth of active sites, thus enhancing the interaction between the metal and the support, which facilitated the adsorption, activation, and transfer of active oxygen, thus promoting the catalytic oxidation performance.

CeO_2 has been widely applied in environmental catalysis due to its high oxygen storage/release efficiency associated with oxygen vacancy formation and its excellent redox behavior resulting from the low redox potential between Ce^{3+} and Ce^{4+}.[7] Especially in vehicle exhaust gas elimination, CeO_2 is a

[a] Q. Liu, P. Yang, W. Tan, Y. Haowei, J. Ji, C. Wu, Y. Cai, F. Gao, L. Dong
State Key Laboratory of Pollution Control and Resource Reuse
School of Environment; Jiangsu Key Laboratory of Vehicle Emissions Control
Center of Modern Analysis; Key Laboratory of Mesoscopic Chemistry of MOE
School of Chemistry and Chemical Engineering, Nanjing University
Nanjing 210023 (China)
E-mail: gaofei@nju.edu.cn

[b] S. Xie, F. Liu
Department of Civil, Environmental, and Construction Engineering
Catalysis Cluster for Renewable Energy and Chemical Transformations (REACT)
NanoScience Technology Center (NSTC), University of Central Florida
Orlando, FL 32816 (United States)

[c] S. Hong
College of Materials Science and Engineering
Beijing University of Chemical Technology, Beijing 100027 (China)

[d] K. Ma
Analysis and Testing Center, Southeast University, Nanjing 211189 (China)

Supporting information for this article is available on the WWW under https://doi.org/10.1002/chem.202203432

commonly used support and an essential component of oxygen storage materials in automotive exhaust control catalysts.[8] It is widely reported that the structural modification of ceria lattice by doping with transition metal cations may enhance the number of defects, the oxygen supply capacity, and lattice oxygen mobility.[9] For instance, an efficient H_2-activation Pt/$CeZrO_x$ (Pt/CZO) catalyst for the catalytic oxidation of CO and C_3H_6 at low temperature by controlling the surface defect sites by doping Zr, which has a smaller ionic radius of Zr^{4+} compared with Ce^{4+}, was reported. The activated Pt/CZO catalyst obtained more exposed active Pt sites on the smaller clusters surrounded by more oxygen defects and Ce^{3+} species.[6] In addition, doping with variable valence metal ions can further affect the oxygen vacancy properties of cerium oxide since the electron can easily be exchanged between cerium and the variable valence metal, which is beneficial for their catalytic activities. Yao et al. reported that incorporating Sn^{4+} into the lattice of CeO_2 was conducive to the enlargement of surface Ce^{3+} content and the formation of oxygen vacancies in the reaction process, which further promoted the enhancement of catalytic performance.[10] Hegde et al. reported that Pd/$Ce_{1-x}Sn_xO_2$ could be a better OSC■■Please define OSC■■ material for low-temperature catalysis compared to Pd/CeO_2, Pd/$Ce_{1-x}Zr_xO_2$, and Pd/$Ce_{1-x}Ti_xO_2$, owing to the two electrons exchange between Ce^{4+}/Ce^{3+} and Sn^{4+}/Sn^{2+} redox couples through the redox equilibrium of $2Ce^{3+} + Sn^{4+} \leftrightarrow 2Ce^{4+} + Sn^{2+}$.[11] Neyman et al. further reported that modification with Sn led to the increased thermal stability of Pt/CeO_2 catalysts and generated more reactive oxygen in the catalysts, thus enhancing the CO oxidation activity in the low-temperature regime.[12] Nevertheless, to the best of our knowledge, no comparative study on surface defect engineering on CeO_2 support by Sn doping for tuning the local structure of Pt species and their application in the catalytic oxidation of CO has been reported.

In the present work, a facile defect engineering strategy for CeO_2 by Sn doping had been successfully developed. Increased surface defects and Ce^{3+} concentration had been achieved on the CSO supports compared with CeO_2. Upon a simple reductive activation by CO, the firmly anchored Pt single sites on Sn-doped CeO_2 were transformed into highly active Pt clusters, outperforming the Pt/CeO_2 catalyst for CO and C_3H_8 oxidation at low temperatures. The impact of Sn doping on the microstructure and catalytic oxidation performance of Pt–CeO_2-based catalyst was systematically investigated using a series of characterization techniques, which revealed a detailed process of structural transformation of Pt single sites into robust Pt clusters under a reduction atmosphere.

Results and Discussion

The CO oxidation activity of the prepared Pt/CeO_2 and Pt/CSO catalysts were illustrated in Figure 1a. It could be seen that initially, there was barely any difference in the performance of the CO oxidation catalytic reaction between the pristine Pt/CSO and Pt/CeO_2 catalysts, which was expected to be due to the high dispersion of Pt on the surface before activation, thus affecting the activity in general. Nevertheless, the catalytic oxidation performance improved after being activated with 8% CO at 275 °C. In this case, the CO oxidation activity of Pt/CSO-a was enhanced to a greater extent than that of Pt/CeO_2, with a drop of 119 °C (from ca. 213 to 94 °C) in T_{50} (where CO conversion reaches 50%) compared with a decline of 90 °C (from ca. 213 to 123 °C) for Pt/CeO_2-a (Figure 1a).

In order to explore whether the extraordinary catalytic performance of the Sn-doped sample was from the contribution of SnO_2, the activity of the Pt/SnO_2 activated sample was tested (Figure 1b). It can be observed that Pt/SnO_2-a exhibited limited CO oxidation activity, suggesting that Pt-SnO_2 species were not reactive in CO oxidation reaction. Based on this, it was proposed that the distinct activity enhancement of Pt/CSO-a compared to Pt/CeO_2-a and Pt/SnO_2-a is related to specific changes in the structure of ceria induced by Sn doping, as well as the strength of Pt–Ce interactions. In addition, the long-term stability test and active cycling experiments suggested that Pt/CSO-a exhibited relatively stable catalytic activity in response to actual working conditions (Figure 1c,d). In summary, Pt/CSO-a is an efficient catalyst with high catalytic oxidation activity and thermal stability. A detailed characterization of these samples was performed to understand the reasons for the different catalytic properties, and the results were presented and discussed in the subsections.

The structural and textural features were first studied to approach the decisive reasons for the significant behavior of doped catalysts. The crystal structure of supports and Pt deposited samples were characterized by powder XRD, and the results were shown in Figure 2a. Like our previous reports,[10] the XRD patterns of CeO_2 and CSO mainly showed the typical cubic fluorite structure CeO_2 (JCPDS 43-1002). Moreover, no diffraction peaks corresponding to SnO_2 were observed in the case of the high-angle shifting of the diffraction peaks of CSO (Figure 2b), indicating that Sn^{4+} has been successfully incorporated into the lattice of CeO_2 to form uniform solid solutions maintaining the fluorite-type structure.[13] In addition, the intensity of the diffraction peaks for CSO was much lower and broader than that of CeO_2, suggesting that CSO possessed a smaller grain size than CeO_2, as confirmed by the grain size of these samples calculated from the diffraction peaks in the (111) plane using the Debye-Scherrer equation (Table 1), mainly due to grain growth was prevented by the lattice of Sn^{4+} doped CeO_2.[14]

Table 1. Crystalline size and specific surface area for the supports and Pt catalysts.

Sample	Crystallite size [nm][a]	Specific area [$m^2 g^{-1}$][b]
CeO_2	12.7	52.9
CSO	9.8	68.8
SnO_2	11	22.8
Pt/CeO_2	11.2	52.8
Pt/CSO	9.0	63.8

[a] The crystallite size was calculated by the Scherrer equation using CeO_2 (111). [b] The specific areas of prepared samples were measured by N_2 physisorption at −196 °C.

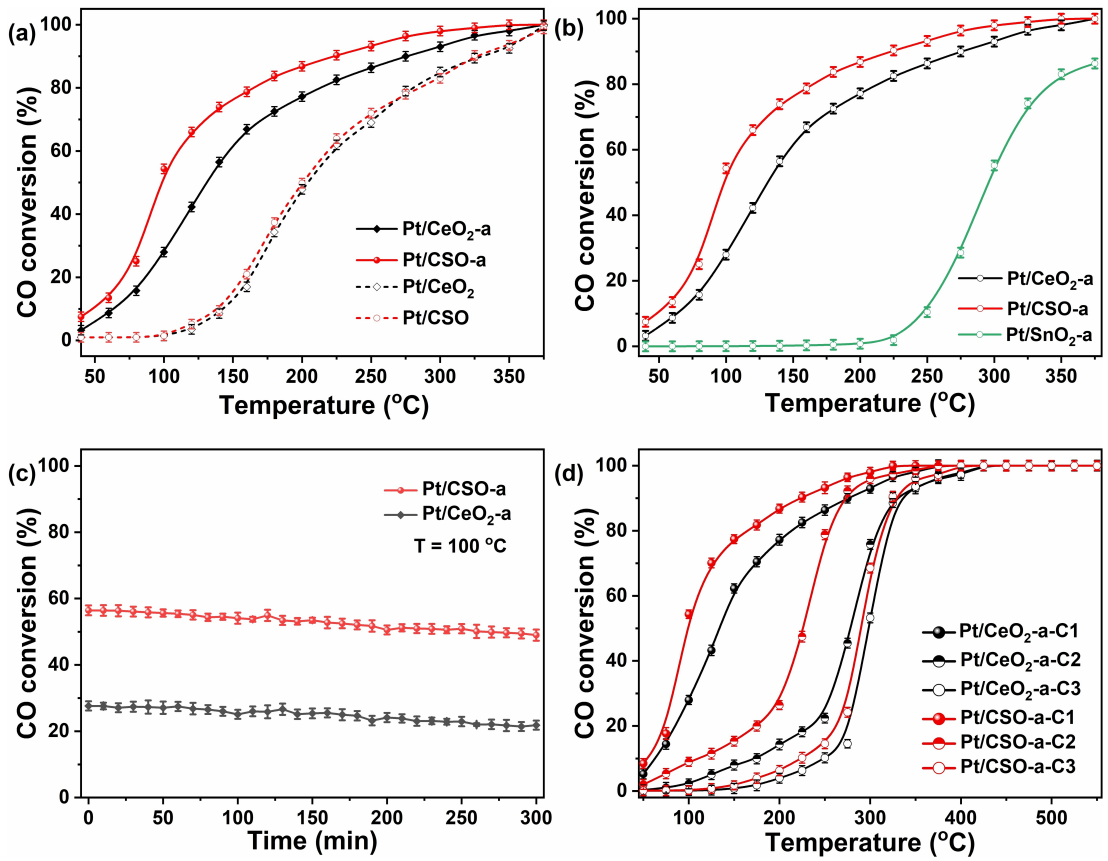

Figure 1. CO oxidation activities on (a) and (b) catalysts that were activated with 8 % CO at 275 °C; Reaction conditions: [CO] = [O_2] = 1 %, He as balance. WHSV = 200,000 mL $g^{-1}h^{-1}$; (c) stability test at 100 °C; (d) activity cycling experiment (from 20 to 550 °C).

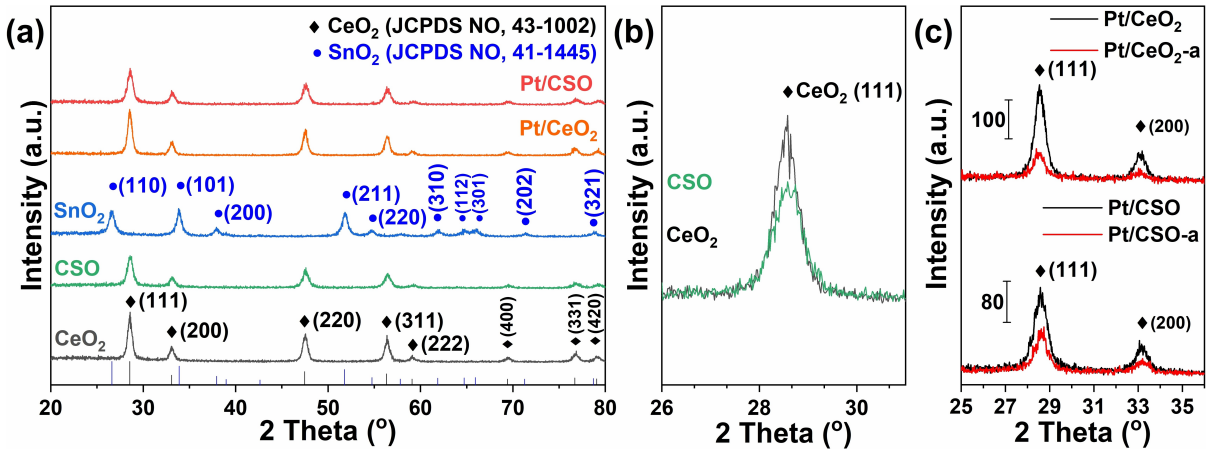

Figure 2. (a) XRD patterns for CeO_2, SnO_2, CSO, Pt/CeO_2 and Pt/CSO (from 20° to 80°); (b) XRD patterns for CeO_2 and CSO (the crystalline surface spacing of CeO_2, (111)); (c) XRD patterns of fresh samples and activated samples (from 25° to 35°).

Following the deposition of Pt on CeO_2 and CSO, the XRD results showed no noticeable difference from the pristine samples, indicating that Pt was highly dispersed on both CeO_2 and CSO. Similar results were obtained for the activated samples, suggesting that the activation process results in no formation of large Pt particles, which remained below the XRD detection limit. However, the intensity of XRD peaks of Pt/CeO_2 and Pt/CSO were reduced after activating, signifying that the activation process degraded the crystallinity of CeO_2 and CSO (Figure 2c). This is probably related to the production of more reduced species (Ce^{3+}) on the surface (to be discussed in our subsequent surface characterization results). Meanwhile, Pt/CeO_2 had a higher drop in peak than Pt/CSO, possibly due to the role of Sn as a variable element in stabilizing the Ce^{3+}

structure. These findings implied the growth of CeO_2 size during the activation process. While the crystallinity of the samples gradually decreased with increasing Sn doping rate, segregation was also observed on $Pt/Ce_xSn_{1-x}O_2$ samples with higher doping rates due to the strong interaction between Pt and CeO_2 (Figure S1).

The specific surface area of the catalysts reflected the contact area with the reacting molecules, thus affecting the catalytic reaction performance, which was also measured (Table 1). The CSO exhibited a higher specific surface area than the CeO_2 ($68.8\ m^2 g^{-1}$ vs. $52.9\ m^2 g^{-1}$). Furthermore, since all samples used the same synthesis method and underwent the same calcination process, it was inferred that the small amount of Sn doping increased the concentration of surface defects in CeO_2, resulting in a larger surface area of the prepared catalyst. Following the deposition of Pt on CeO_2 and CSO, the specific surface area results showed no noticeable difference from the pristine samples, indicating that Pt was highly dispersed on both CeO_2 and CSO. These results collectively indicated that samples with a uniform size (ca. 10 nm) and higher specific surface area were successfully prepared, improving catalytic applications' versatility.

To further prove this idea, HR-TEM was first used to verify the dispersion of Sn and Pt in CeO_2. As illustrated in Figure S2a, b, only the crystalline CeO_2 can be seen in the results, where the crystalline surface spacing of the sample can be measured corresponding to the typical CeO_2 cubic fluorite structure, such as 0.280 nm and 0.314 nm correspond to the crystalline surface spacing of the (200) and (111) surfaces of CeO_2, respectively. This proved that Pt was uniformly dispersed on the surface of the support. Considering that the Pt particulate size plays a significant role in determining the catalytic oxidation performance of CO oxidation,[15] HAADF-STEM and EDS mapping were performed to verify the dispersion of Pt active species on the support surface and visualize the particle size of the active species. As shown in Figure 3b, Sn was uniformly distributed in CeO_2, further supporting the XRD results. More focus on the dispersion of the active species on the surface and the aggregation of Pt clusters on the support surface can be seen in Figure 3a, b and Figure S2c, d. After activation, Pt species migrated on the support surface, and the brighter clusters or dots could be attributed to the formation of aggregated Pt species. To further compare the dispersion of Pt species on Pt/CeO_2-a and Pt/CSO-a, the average Pt cluster size on these two samples was calculated (Figure 3a, b). The Pt clusters of Pt/CSO-a were significantly smaller (1.2 ± 0.3 nm) than Pt/CeO_2-a (1.9 ± 0.3 nm), and the size distribution on Pt/CSO-a was narrower and more uniform. Pt migrated on the support surface due to the solid Pt–CeO_2 interaction, while the abundance of defect sites should be facilitated the formation of more uniform and smaller Pt clusters (Figure 3(B) III). Interestingly, the average Pt cluster size on Pt/CSO-a (1.2 ± 0.3 nm) was very close to the previously reported optimal Pt cluster size, where CeO_2-supported Pt clusters with an average diameter of ca. 1.4 nm were just large enough to efficiently activate CeO_2 redox chemistry and provide abundant active interfacial sites for CO oxidation.[15] The reasons for the agglomeration phenomenon of Pt on different support surfaces, associated with the surface conditions, will be discussed below.

As mentioned before, oxygen vacancies on the support surface contributed significantly to the particle size of Pt species,[6,16] so the oxygen vacancies have been studied and explored in depth. Raman spectroscopy is a standard method to characterize oxygen vacancies on the surface of cerium oxide. An intense peak at ca. $465\ cm^{-1}$ represented the Raman spectrum of CeO_2-based materials due to the fluorite structure's F_{2g} Raman activity mode. In addition, a shoulder peak was observed at ca. $600\ cm^{-1}$, which was associated with oxygen vacancies in CeO_2.[17] As illustrated in Figure 4a, the data were first normalized based on the peaks at $465\ cm^{-1}$. The intensity of the $595\ cm^{-1}$ peaks could be considered to reflect the concentration of oxygen vacancies on the sample surface. The corresponding peak intensity at $595\ cm^{-1}$ in CSO was significantly more robust than CeO_2, which pointed to the construction of more surface defects by doping Sn into CeO_2. In the meantime, EPR was used to directly detect the effect of Sn

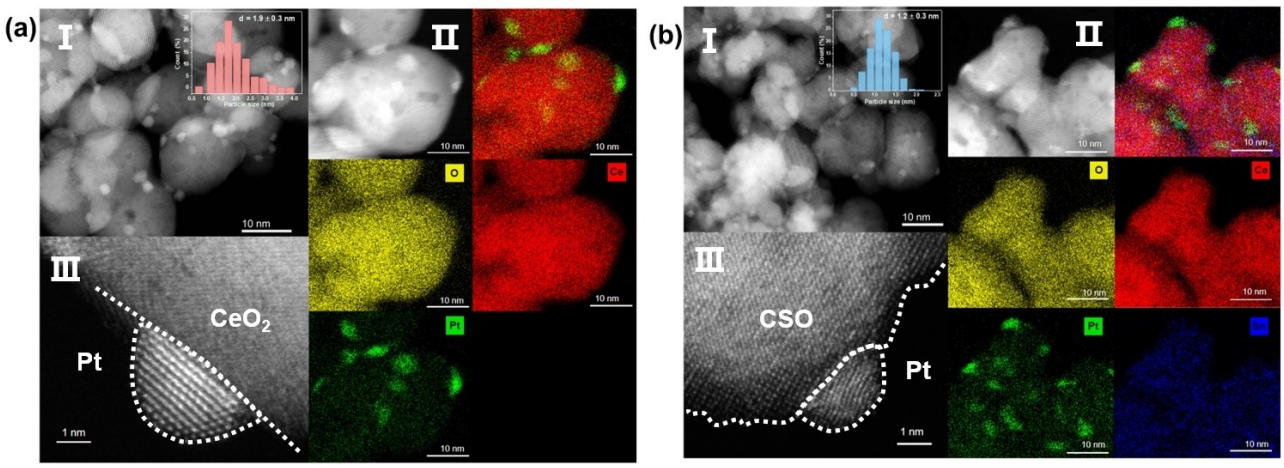

Figure 3. HAADF-STEM images and EDS mapping results of (a) Pt/CeO_2-a and (b) Pt/CSO-a (The number of particle size statistics was more than 500).

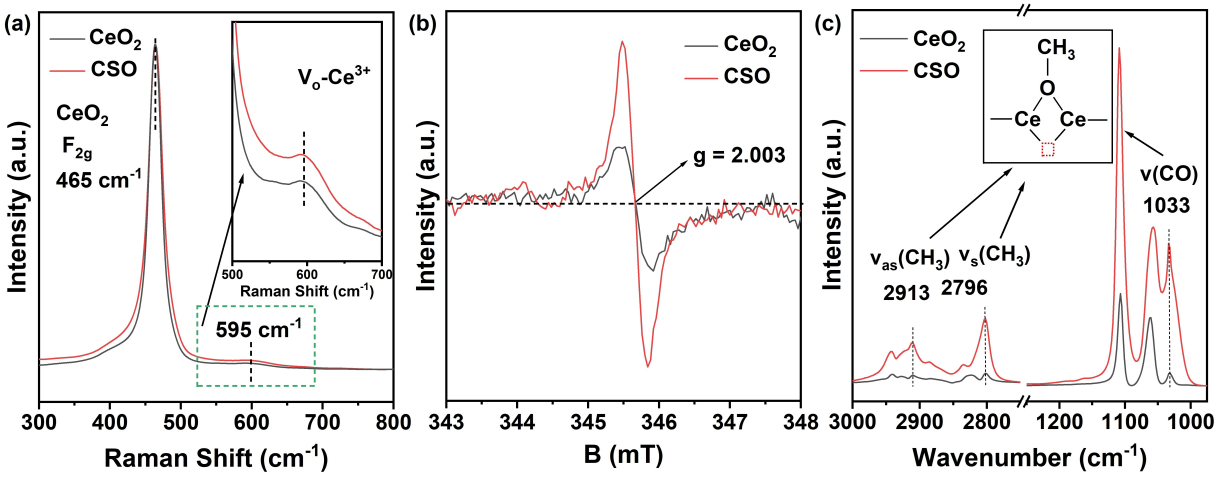

Figure 4. (a) Raman spectra of CeO_2 and CSO; (b) EPR spectra of CeO_2 and CSO; (c) in situ DRIFTS of methanol adsorption on CeO_2 and CSO at 30 °C.

addition on oxygen vacancies on the catalyst surface by comparing the intensity of the oxygen vacancy spectrum at the *g* value of 2.003.[18] As shown in Figure 4b, the much stronger resonance line intensities on CSO than that on CeO_2 indicate the formation of more oxygen vacancies on CSO. In situ DRIFTS of the methanol adsorption on CeO_2 and CSO at 30 °C were carried out to verify this viewpoint further. Concerning the spectral features in the region of 2700–3000 cm^{-1} and 1000–1200 cm^{-1}, three IR peaks at 1033 cm^{-1}, 2796 cm^{-1}, and 2913 cm^{-1} can be observed, which were attributed to bridged methoxy species associated with an oxygen vacancy exists between the two bridged Ce ions.[19] The intensities of these three bands on CSO were more intense than those on CeO_2, further indicating that more surface oxygen vacancies were indeed formed on the CSO support.

Oxygen vacancy restriction of Pt growth was principally due to the regulation of Pt-support interactions, allowing for drastic changes in Pt structure during the activation process. As reported elsewhere, the CO oxidation activity of both Pt/CeO_2 and Pt/CSO catalysts was substantially increased after CO activation, indicating that the surface structure of the catalysts underwent a significant structural evolution during the activation process.[5b,6, 20] To investigate the reasons for structural evolution, Raman spectra of catalysts were collected for two periods in Figure 5a,b. After the deposition of Pt, two new bands at 547 and 648 cm^{-1} emerged, which could be attributed to Pt–O–Ce and Pt–O (in Pt–O–Ce) structure, respectively.[21] The higher intensity of bands at 547 and 648 cm^{-1} indicated that more Pt–O–Ce linkages were formed on Pt/CSO, which might be related to the higher dispersion of Pt on CSO due to the increase of surface oxygen vacancies. The intensity of the two bands assigned to Pt–O–Ce and Pt–O structure declined dramatically after CO activation, which could be attributed to the depletion of Pt–O bonds and the formation of metallic Pt clusters. Interestingly, all the samples after CO activation showed prominent surface adsorption oxygen vibration peaks at 828 cm^{-1}, assigned to peroxo-like species, proving that the structure evolved drastically during Pt cluster formation and the presence of oxygen vacancies allowed for better oxygen activation by the catalysts (Figure 5b).[22] Furthermore, the peak intensity of these species was significantly greater in Pt/CSO-a than in Pt/CeO_2-a, showing that Pt/CSO-a was more conducive to the activation of oxygen species and, thus, more efficient for the catalytic oxidation of CO.

To further demonstrate the structural evolution of catalysts in reductive activation treatment, H_2-TPR and CO-TPR experiments were performed. For H_2-TPR results, the overall reduction profiles can be divided into low to high-temperature zones corresponding to the reduction of surface O species, surface CeO_2, and bulk CeO_2, respectively.[23] With the doping of Sn, there was a significant forward shift of the low-temperature broad H_2-consumption peak (from 410 to 294 °C) in the H_2-TPR profile of CSO (Figure S3). This also explained the higher mobility of oxygen on the surface of the support compared with CeO_2 and SnO_2 due to the electronic interactions produced by the Ce^{4+}/Ce^{3+} and Sn^{4+}/Sn^{2+} redox equilibrium through $2Ce^{3+} + Sn^{4+} \leftrightarrow 2Ce^{4+} + Sn^{2+}$. In order to demonstrate the effect of the CO activation process on the redox properties of the samples, CO-TPR experiments were performed using the reactant CO. After the Pt deposition (Figure 5c), the CO consumption peaks below 250 °C were attributed to the reduction of oxygen close to the Pt–O and Pt-support interface, respectively, which was considered effective in improving the reducibility of Pt-based catalysts.[24] To verify this idea, the CO-TPR results regarding the Pt-support interface were fitted with a split-peak fit, as shown in Figure 5c. Comparing the position and area of CO consumption peaks of these species at low temperatures (112 °C to 104 °C), very little difference was found between them (Table S2). This exciting phenomenon may explain the slight difference in the catalytic performance of the catalysts before the activation treatment. After the CO activation treatment (Figure 5d and Table S2), both Pt/CeO_2 and Pt/CSO showed a considerable improvement in the reducibility, regardless of the low-temperature (< 350 °C) reducibility or the total amount of CO consumption. Moreover, The CO consumption peaks assigned to the reduction of Pt–O–Ce on Pt/CSO

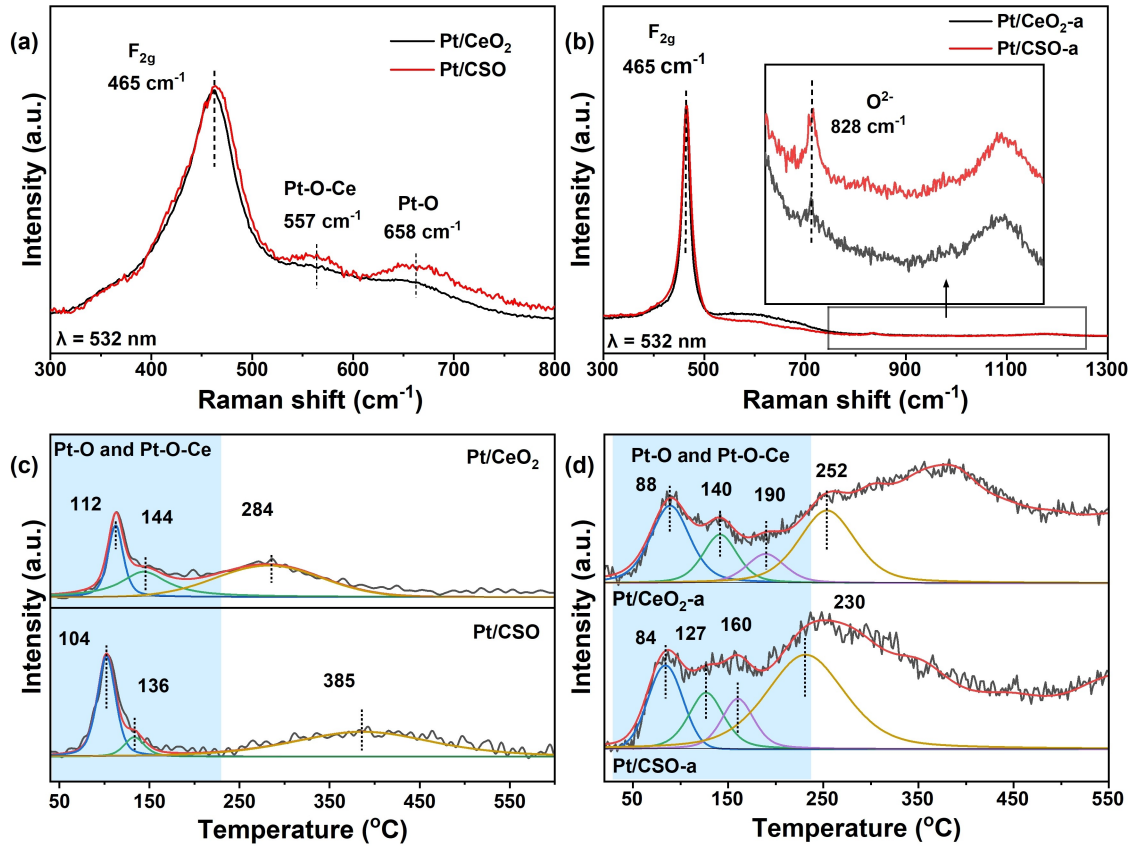

Figure 5. Raman spectra of (a) fresh Pt/CeO_2 and Pt/CSO; (b) activated Pt/CeO_2-a and Pt/CSO-a (The height of the CeO_2 F_{2g} band for various samples was normalized.); (c) CO-TPR profiles of Pt/CeO_2 and Pt/CSO; (d) CO-TPR profiles of Pt/CeO_2-a and Pt/CSO-a.

structures were much more intense than those on Pt/CeO_2 counterparts, suggesting the formation of more active species on CSO after activation. This result demonstrated that the Pt/CSO surface underwent a more drastic change during the reduction process. This was most likely due to the more abundant oxygen vacancies on the CSO surface exposing more Pt–O–Ce interfaces on the highly dispersed Pt on the support during the activated agglomeration. Combined with the statistics of the electron microscopy results above, it could well be the result of the Pt cluster size effect.

XPS experiments were conducted to reveal the surface chemical state of CeO_2 and CSO before and after activation of Pt/CeO_2 and Pt/CSO. The concentrations of surface elements were listed in Table S3. The reduced concentration of Pt on the surface of the activated samples should be due to the agglomeration of Pt on the support surface, in agreement with the previous TEM results. The XPS spectra of all samples were shown in Figure S4, and the results of their deconvolution were presented in Figure 6. It can be seen clearly that Pt species mainly existed in the form of $Pt^{\delta+}$ before activation and were dominated by Pt^{2+} and Pt^{4+} species in Pt/CeO_2 and Pt/CSO, respectively. It was typically assumed that $Pt^{\delta+}$ was associated with the dispersion of Pt, representing the presence of Pt on the surface in the form of the oxidation state of Pt.[25] A higher concentration of $Pt^{\delta+}$ on the Pt/CSO surface was consistent with the previously mentioned conclusion that surface oxygen vacancies were associated with favorable Pt dispersion. After activation, the peaks assigned to Pt $4d_{5/2}$ and Pt $4d_{3/2}$ shifted to lower binding energy, accounting for the formation of Pt metal species[26] Interestingly, Pt agglomeration occurred on the support surface after activation of CO, and the ionic state was rapidly consumed. As shown in Figure 6a, Pt/CSO exhibited a higher concentration of Pt^0. The concentration of Pt0 on the Pt/CSO-a surface was much higher than that on the Pt/CeO2-a (70.8% vs. 56.0%), which could be due to the smaller Pt clusters exposing more Pt0 on the surface. The enhancement of activity may be related to the appearance of the metallic state Pt^0. In combination with the above oxygen vacancy analysis, it was deduced that the presence of oxygen vacancies could limit the agglomeration of Pt on the support surface, resulting in the formation of Pt clusters with smaller sizes.

As shown in Figure 6(b), the Ce^{3+} concentration on the CeO_2 surface increased from 21.3% to 24.1% after doping with Sn^{4+} (smaller ionic radius, r = 0.071 nm) due to lattice shrinkage/deformation and spontaneous conversion of Ce^{4+} (r = 0.092 nm) to Ce^{3+} (r = 0.103 nm). To maintain the charge balance, more oxygen vacancies were formed accordingly. This viewpoint was well supported by the results of Raman spectra (Figure 5(a)). After the Pt deposition, the surface Ce^{3+} decreased dramatically, resulting from the reaction between PtO_2 and

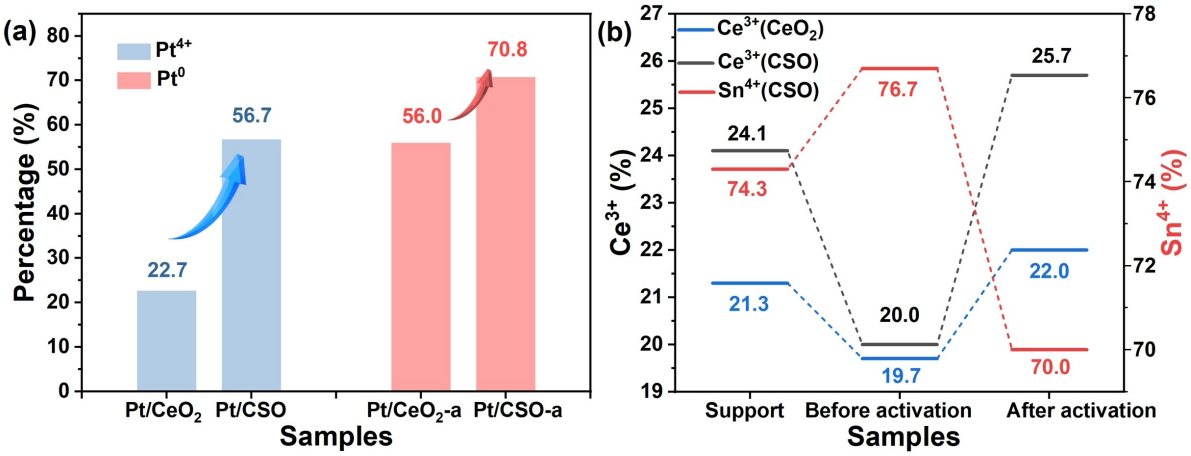

Figure 6. Changes in the ratio of (a) Pt^{4+} and Pt^{0} ;(b) Ce^{3+} to Sn^{4+} in XPS.

Ce^{3+} ($PtO_2 + 2Ce^{3+} \rightarrow Ce^{4+}–O–Pt^{2+}–O–Ce^{4+}$).[27] After CO activation, due to the reduction of Pt–O–Ce structure, as demonstrated in Figure 6(b), the concentration of surface Ce^{3+} on both Pt/CeO_2 and Pt/CSO increased significantly. The relatively higher surface Ce^{3+} on Pt/CSO-a could be related to the formation of more Pt–O–Ce linkages and stronger $Pt–CeO_2$ interactions on Pt/CSO compared to Pt/CeO_2. Considering that the smaller Pt clusters on Pt/CSO-a could help generate more $Pt–CeO_x$ interface and expose more Pt sites, it could be proposed that more surface oxygen vacancies/Ce^{3+} at or near the Pt cluster-CeO_2 perimeter sites could significantly promote the activation of reactants. According to the literature, Sn doping into CeO_2 can modulate the electronic state of Ce through $Ce^{3+} + Sn^{4+} \leftrightarrow 2Ce^{4+} + Sn^{2+}$.[9c,11, 13b] The Sn 3d XPS of prepared samples was shown in Figure S4b. The proportions occupied by Sn^{4+} and Ce^{3+} in their respective elements always maintained an opposite trend, regardless of the deposition of Pt or the activation of CO (Figure 6b). This was due to Ce^{4+}/Ce^{3+}, Sn^{4+}/Sn^{2+} redox couples, and Sn played a buffering role in the redox cycle of Ce.

In situ DRIFTS of CO adsorption and subsequent oxidation were performed to identify the active sites on these two activated catalysts. As shown in Figure 7a,b, three distinctive bands were observed on both catalysts after the activation. The band at high frequency (ca. 2103 cm^{-1}) was assigned to CO adsorbed on ionic Pt at the interface between Pt clusters and CeO_2 (CO–$Pt^{\delta+}$@clusters), while the bands at ca. 2084 cm^{-1} and 2066 cm^{-1} were assigned to the collective oscillation of CO on metallic Pt clusters (CO–Pt^{0}@clusters) with the under coordinated (UC, 7–8-fold coordinated) and highly undercoordinated (H-UC, $\leq$6-fold coordinated) Pt sites, respectively.[28]

To further evaluate the reactivity of CO adsorbed on the catalyst, the IR spectra were collected by N_2 purging (N_2 flow for 30 min) and O_2 injecting (O_2 flow for the 60s). The IR band's intensity, corresponding to CO–Pt^{0}@clusters, decreased rapidly, while the IR band, corresponding to CO–$Pt^{\delta+}$@clusters, remained unchanged after the introduction of O_2. These changing trends represented that Pt^{0} sites with smaller particle sizes were the active sites. And the corresponding reactivity order was CO–Pt^{0}@clusters > CO–$Pt^{\delta+}$@clusters. Furthermore, the percentage change of the integrated areas of the peaks belonging to CO–Pt^{0}@clusters in the first 60 s of the O_2 purge was shown in Figure 7c, where the CO–Pt^{0}@clusters on Pt/CSO-a decreased more rapidly when oxygen is passed for a more extended period. It was inferred that the smaller particle size of Pt^{0} might have more UC sites with the same loading, which led to the rapid reaction of CO on the surface and thus exhibited better catalytic performance.

To investigate the differences in the activity of the low-temperature phase, kinetic characterization of the low-temperature section of CO oxidation was first done in performed (Figure 7d,e). The conversion rate was selected at around 10% of the temperature to eliminate the effect of internal and external diffusion. The above kinetic results of reaction orders confirmed the vital role of O_2 activation on Pt sites. Since the reaction order of CO was close to zero for both Pt/CeO_2-a and Pt/CSO-a, the adsorption of CO did not contribute much to the activity at low temperatures. In other words, the activation of O_2 could be the rate-determining step. The higher O_2 reaction order on Pt/CSO-a compared to that on Pt/CeO_2-a indicated that O_2 could be better activated on Pt/CSO-a, which was well corroborated with the results of in situ DRIFTS of adsorbed CO reacting with O_2 (Figure 7a,b)

The activation capacity of oxygen can be more visually demonstrated by the oxygen storage capacity (OSC), which is one of the most significant indices for evaluating the redox properties of catalysts for vehicle exhaust purification, and it is also a means of visually detecting the strength of the catalyst for oxygen activation.[29] The dynamic OSC of Pt/CSO-a and Pt/CeO_2-a were tested (all catalysts were activated by CO at 275 °C for 1 h before testing), and the results were shown in Figure 8a. Pt/CSO-a exhibited higher OSC values than Pt/CeO_2-a at different temperatures after CO activity treatment. This supported the previously mentioned point that Pt/CSO-a has a significantly better oxygen activation capacity than Pt/CeO_2-a. To better confirm the correlation between CO oxidation activity and OSC

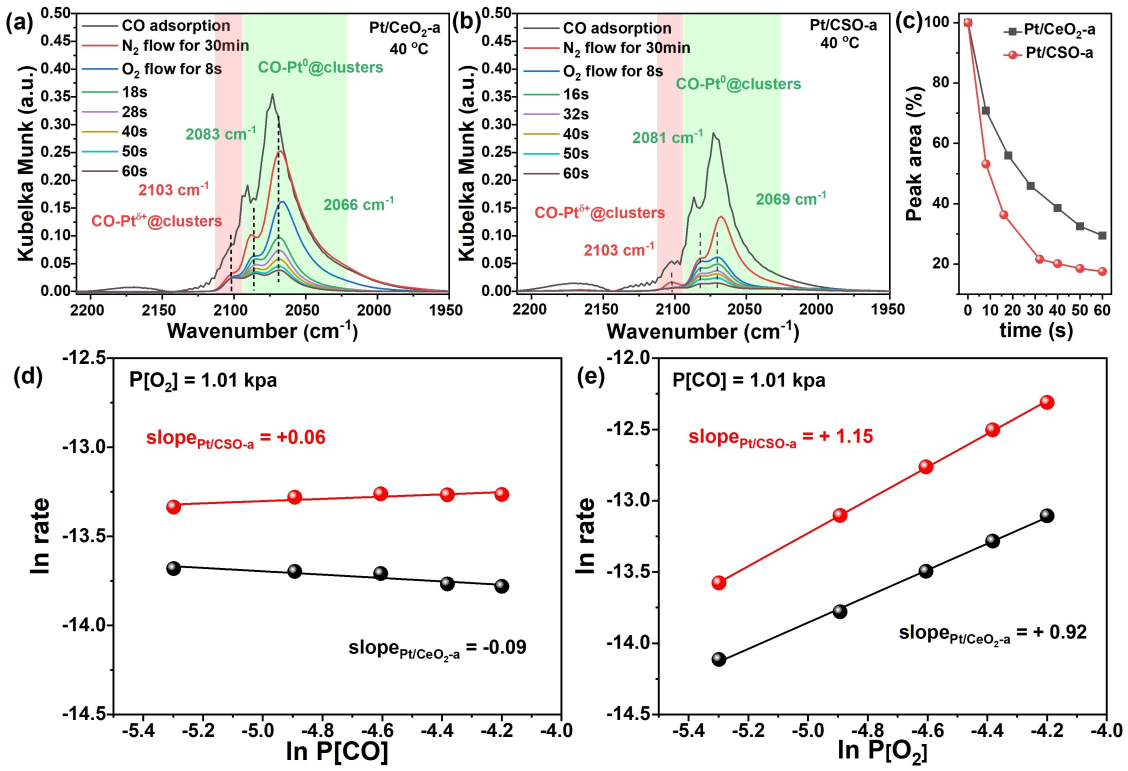

Figure 7. CO adsorption and reaction between O_2 and adsorbed CO on (a) Pt/CeO_2-a; (b) Pt/CSO-a monitored by in situ DRIFTS; (c) Percentages of the integrated area of CO–Pt^0@clusters after O_2 pulses at 40 °C; Reaction orders for (d) CO and (e) O_2 in CO oxidation reaction on Pt/CeO_2-a and Pt/CSO-a. The rate of CO reaction can be described as $r = k[CO]^x[O_2]^y$, with *x* and *y* being constants.

values, both were shown together in Figure 8b. As the OSC value increases, the conversion of CO is also elevated, exhibiting an approximately linear relationship, which suggested that the adsorption and activation of oxygen were vital for the catalytic oxidation of CO. Experiments using the TWC reaction for propane oxidation were performed to investigate this idea. As shown in Figure S5, Pt/CSO-a also performed better than Pt/CeO_2-a in the C_3H_8 oxidation reaction. This confirmed the idea that Pt/CSO-a structure also favored propane's oxidation reaction, probably due to its more remarkable ability to activate oxygen.

In previous research, it was widely recognized that the CO oxidation reaction on Pt/CeO_2 catalysts primarily followed a Mars-van Krevelen (MvK) mechanism, in which CO adsorbed on Pt sites reacted with activated lattice oxygen. At the same time, activation of oxygen on-oxygen vacancies was the rate-determining step.[30] The results of OSC testing confirmed that the CO oxidation reaction on Pt/CSO catalysts also proceeded in the MvK mechanism. In short summary, as shown in Figure 8c, the doping of Sn could induce the generation of more oxygen vacancies on the surface of CeO_2 and thus enhance its redox ability. The presence of oxygen vacancies limited the growth of Pt clusters during activation, resulting in smaller cluster species with a greatly enhanced ability to activate oxygen.

Conclusion

In a nutshell, a Pt/CSO catalyst for the catalytic oxidation of CO was designed and studied systematically to improve the performance of the oxidative process at low temperatures. Through a facile SnO_2 doping method, more surface defects and Ce^{3+} species were created on the CSO support, which limited the particle size of the active Pt clusters, thereby promoting the catalytic performance of the supported catalysts. Although the firmly anchored Pt single sites exhibited limited CO oxidation activity, the CO oxidation activity of the activated Pt/CSO catalyst was higher than that of the Pt/CeO_2 catalyst after CO activation. It was concluded that much smaller Pt clusters could be formed on the activated Pt/CSO catalysts, with more exposed Pt sites for CO adsorption and more abundant Pt–CeO_2 perimeter active sites. This work provides a facile but effective strategy for fabricating a uniform Pt cluster-based oxidation catalyst, which may help to design an efficient CO oxidation catalyst with superior activity at low temperatures.

Experimental Section

Catalyst preparation

The CeO_2 and $Ce_xSn_{1-x}O_2$ supports were prepared by a precipitation method using $NH_3{\cdot}H_2O$ as the precipitator. A requisite quantity of

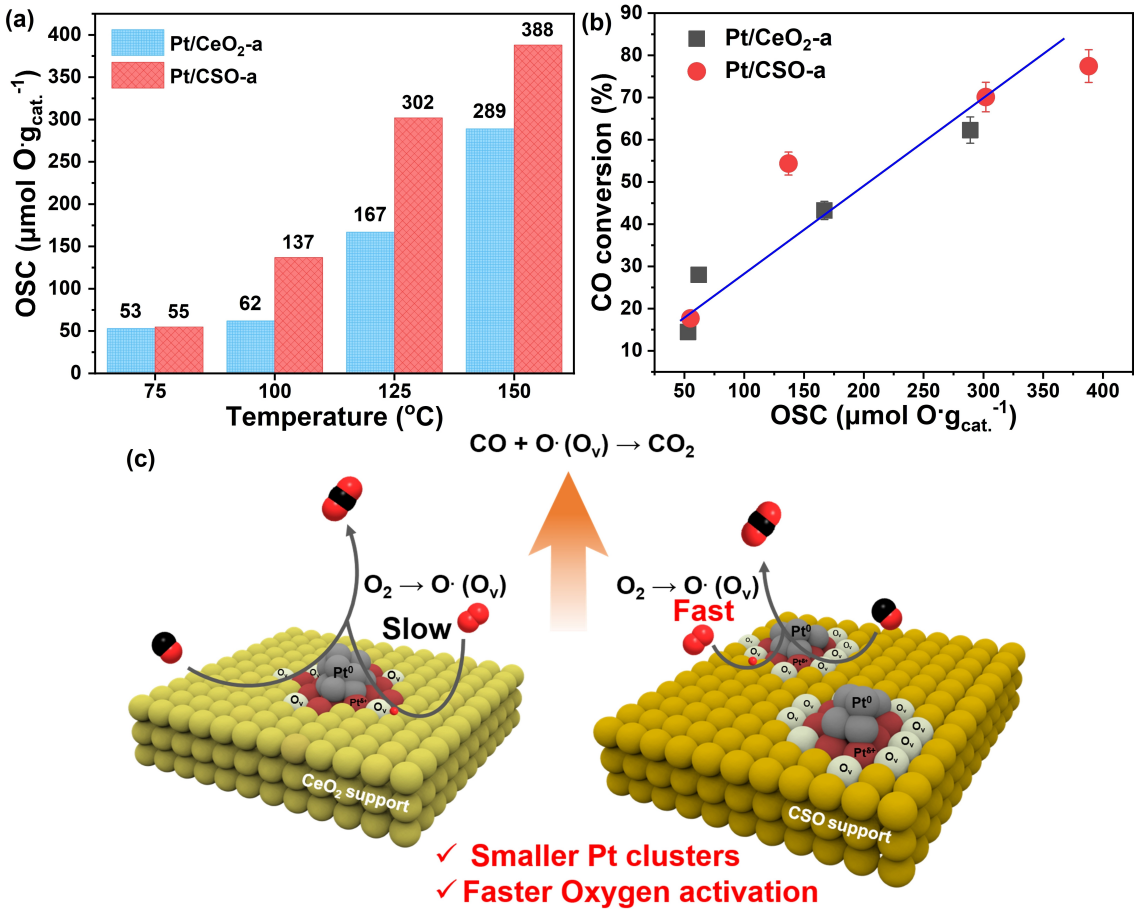

Figure 8. Results of OSC measurement. (a) OSC values of Pt/CeO_2-a and Pt/CSO-a;(b) The relationship between CO conversion and OSC functions on Pt/CeO_2-a and Pt/CSO-a. (c) The structure-activity relationship of CO oxidation on Sn-doped Pt/CeO_2 catalysts.

$Ce(NO_3)_3 \cdot 6H_2O$ was dissolved in deionized water. Then an excessive amount of $NH_3 \cdot H_2O$ aqueous solution was dropwise added into the solution until pH reached 10. The resulting mixtures were aged at room temperature for 10 h. Afterward, the precipitate was washed several times with distilled water until no pH changed and no Cl^- detected by the solution of $AgNO_3$ and then dried at 100 °C for 12 h. The CeO_2 support was obtained by subsequent calcination in air at 550 °C for 4 h, with a ramping rate of 2 °C min^{-1}. $Ce_xSn_{1-x}O_2$ was prepared by mixing $Ce(NO_3)_3 \cdot 6H_2O$ and $SnCl_4 \cdot 5H_2O$ in the same way.

Pt ($Pt(NO_3)_2$ as a precursor) was loaded on CeO_2 and $Ce_xSn_{1-x}O_2$ (Pt/CeO_2 and Pt/CSO) using the incipient wetness impregnation (IWI) method (The mass fraction of Pt was 1 wt. %). A certain amount of the precursor was dissolved in deionized water and dropwise added onto the prepared support, followed by calcination at 550 °C for 4 h in air. Before the CO oxidation activity test, the samples were reduced with 8% CO/Ar at 275 °C for 1 h, then cooled down to room temperature and flowed with air for 1 h. The activated samples were denoted with "-a" (-a = Activation by CO reduction)

CO oxidation activity evaluation

CO oxidation was a crucial reaction in vehicle emission control and was selected as a probe reaction to evaluate the catalytic performance of Pt/CeO_2 and Pt/CSO catalysts. The CO oxidation activity of prepared samples was tested in a fixed-bed quartz tube reactor at atmospheric pressure at a steady state. The reaction gas contained 1% CO and 1% O_2, He in balance. The flow rate was 50 mL min^{-1} with a weight hourly space velocity (WHSV) of 200,000 mL $g^{-1} \cdot h^{-1}$. The effluent gas was continuously analyzed by a GC-9860 instrument, using an online FID as a detector (detection limit: $\leq 1 \times 10^{-11}$ g·s^{-1} (n-hexadecane); linear range: $\geq 10^6$). CO conversion was calculated as follows:

$$\text{CO conversion} = \frac{[CO_2]_{out}}{[CO]_{in}} \times 100\,\%$$

Catalysts characterization

X-ray diffraction (XRD) measurement patterns were recorded on a Philips X'pert Pro diffractometer using Ni-filtered Cu Kα radiation ($\lambda = 0.15408$ nm). The X-ray tube was operated at 40 kV and 30 mA. The data of 2θ from 10° to 80° were collected with 10° min^{-1}.

N_2 adsorption-desorption isotherms measured the specific surface area of the samples at 77 K on a Quanta chrome Autosorb-iQ instrument. Before testing, all samples were degassed under a vacuum at 200 °C for 2 h. The surface area was determined by Brunauer-Emmett-Teller (BET) methods in the partial pressure range of 0.05 to 0.30.

Raman spectra of the catalysts were collected on a LabRAM Aramis spectrograph with a spectral resolution of 2 cm^{-1}. A 532 nm diode-pumped solid-state semiconductor laser was used as the excitation source with a power output of 30 mW.

The EPR technology identified reactive oxygen species at room temperature on a Bruker EMX spectrometer at a frequency of 10 GHz and a magnetic field of 100 kHz. The g-values were calculated by the relation $g = h\nu \cdot \beta^{-1} \cdot Hr^{-1}$, where h is the Planck constant, J·s; ν is the microwave frequency, s^{-1}; β is the Bohr magneton, $J \cdot T^{-1}$; and Hr is the magnetic field, T.

X-ray photoelectron spectra (XPS) experiments were conducted on a PHI 5000 VersaProbe system, using monochromatic Kα radiation (1486.6 eV) with an accelerating power of 15 kW. The charging effects of samples were compensated by calibrating all binding energies (BE) with the adventitious C 1s peak at 284.6 eV.

H_2-temperature-programmed reduction (H_2-TPR) was performed in a quartz U-tube reactor connected to a thermal conductivity detector (TCD). In a typical measurement, ca. 30 mg of the catalyst was first pretreated in a flow of air at 200 °C for 1 h and then cooled down to room temperature (30 °C). Then the temperature was linearly raised from 30 °C to 750 °C with a ramping rate of 10 °C min^{-1} in a flow of 10 vol % H_2/Ar (30 mL min^{-1}). The signal of H_2 consumption was monitored by a thermal conductivity detector (TCD). H_2O was removed by a cold trap filled with liquid N_2 before the gas mixture passed into the TCD.

In situ diffuse reflectance infrared Fourier transform spectroscopy (in situ DRIFTS) experiments were implemented on a Nicolet Nexus 5700 FTIR spectrometer furnished with an MCT detector cooled by liquid nitrogen. Before the CO adsorption experiments, the samples were activated with pretreated in a flow of 8% CO/Ar at 275 °C for 1 h and then switched to a flow of N_2 at 275 °C for 1 h. And then cooled down to 40 °C. The backgrounds of catalysts were collected in a flow of N_2 at 40 °C and automatically subtracted from the sample spectrum. A flow of 1.6% CO/Ar at 40 °C for 1 h, and then switch the air path, using a flow of N_2 to blow excess CO. All spectra were recorded from 400 cm^{-1} to 4000 cm^{-1} by accumulating 100 scans, with a spectral resolution of 4 cm^{-1}, and the DRIFTS data were presented in the form of Kubelka-Munk.

CO-temperature-programmed reduction (CO-TPR) experiments were carried out on a quadrupole mass spectrometer. In a typical measurement, ca.100 mg of the catalyst was first pretreated in a flow of CO at 275 °C for 1 h and then cooled down to room temperature (30 °C) with a flow of air. Then the temperature was linearly raised from 30 °C to 650 °C with a ramping rate of 10 °C min^{-1} in a flow of 8% CO/Ar (30 mL min^{-1}). A mass spectrometry detector monitored the signal of CO consumption.

The prepared samples' dynamic oxygen storage capacity (OSC) was measured by a 2% O_2 / 4% CO pulse experiment with a pulse interval of 30 s, a total flow rate of 100 mL·min^{-1}, and a sample dosage of 25 mg. Samples were pretreated with an 8% CO/Ar gas stream at 275 °C for 1 h before testing. The outlet gas was routed to an online mass spectrometer (Hiden Analytical, HPR20 R&D) to analyze the composition. The OSC of the samples was calculated from the CO_2 content of the outlet gas.

Acknowledgements

The financial support of from the National Natural Science Foundation of China (No. 21972063) and the Natural Science Foundation of Jiangsu Province (BK20200012) are gratefully acknowledged.

Conflict of Interest

The authors declare no conflict of interest.

Data Availability Statement

The data that support the findings of this study are available in the supplementary material of this article.

Keywords: CO oxidation · oxygen vacancy · Pt clusters · Sn doped CeO_2 · surface structural evolution

[1] A. K. Datye, M. Votsmeier, *Nat. Mater.* **2021**, *20*, 1049–1059.
[2] M. V. Twigg, *Catal. Today.* **2011**, *163*, 33–41.
[3] a) W. Tan, H. Alsenani, S. Xie, Y. Cai, P. Xu, A. Liu, J. Ji, F. Gao, L. Dong, E. Chukwu, M. Yang, F. Liu, *ChemNanoMat* **2020**, *6*, 1797–1805; b) Y. Xin, N. Zhang, Y. Lv, J. Wang, Q. Li, Z. Zhang, *J. Rare Earth* **2020**, *38*, 850–862.
[4] a) F. Maurer, J. Jelic, J. Wang, A. Gänzler, P. Dolcet, C. Wöll, Y. Wang, F. Studt, M. Casapu, J.-D. Grunwaldt, *Nat. Catal.* **2020**, *3*, 824–833; b) Y. Lu, C. Thompson, D. Kunwar, A. K. Datye, A. M. Karim, *ChemCatChem* **2020**, *12*, 1726–1733; c) G. Ferré, M. Aouine, F. Bosselet, L. Burel, F. J. Cadete Santos Aires, C. Geantet, S. Ntais, F. Maurer, M. Casapu, J. D. Grunwaldt, T. Epicier, S. Loridant, P. Vernoux, *Catal. Sci. Technol.* **2020**, *10*, 3904–3917.
[5] a) L. Nie, D. Mei, H. Xiong, B. Peng, Z. Ren, P. Hernandez Xavier Isidro, A. DeLaRiva, M. Wang, H. Engelhard Mark, L. Kovarik, K. Datye Abhaya, Y. Wang, *Science* **2017**, *358*, 1419–1423; b) X. I. Pereira-Hernández, A. DeLaRiva, V. Muravev, D. Kunwar, H. Xiong, B. Sudduth, M. Engelhard, L. Kovarik, E. J. M. Hensen, Y. Wang, A. K. Datye, *Nat. Commun.* **2019**, *10*, 1358; c) S. Gatla, D. Aubert, G. Agostini, O. Mathon, S. Pascarelli, T. Lunkenbein, M. G. Willinger, H. Kaper, *ACS Catal.* **2016**, *6*, 6151–6155; d) A. Liu, X. Liu, L. Liu, Y. Pu, K. Guo, W. Tan, S. Gao, Y. Luo, S. Yu, R. Si, B. Shan, F. Gao, L. Dong, *ACS Catal.* **2019**, *9*, 7759–7768.
[6] W. Tan, S. Xie, Y. Cai, M. Wang, S. Yu, K.-B. Low, Y. Li, L. Ma, S. N. Ehrlich, F. Gao, L. Dong, F. Liu, *Environ. Sci. Technol.* **2021**, *55*, 12607–12618.
[7] a) J. Ji, Y. Tang, L. Han, P. Ran, W. Song, Y. Cai, W. Tan, J. Sun, C. Tang, L. Dong, *Chem. Eng. J.* **2022**, *445*; b) W. Tan, A. Liu, S. Xie, Y. Yan, T. E. Shaw, Y. Pu, K. Guo, L. Li, S. Yu, F. Gao, F. Liu, L. Dong, *Environ. Sci. Technol.* **2021**, *55*, 4017–4026; c) J. Ji, M. Jing, X. Wang, W. Tan, K. Guo, L. Li, X. Wang, W. Song, L. Cheng, J. Sun, W. Song, C. Tang, J. Liu, L. Dong, *J. Catal.* **2021**, *399*, 212–223; d) Z. Shen, Y. Zhou, Y. Guo, J. Zhao, J. Song, Y. Xie, Y. Ling, W. Zhang, *Chin. Chem. Lett.* **2021**, *32*, 2524–2528.
[8] J. Yang, N. Yigit, J. Moller, G. Rupprechter, *Chem. Eur. J.* **2021**, *27*, 16947–16955.
[9] a) W. Tan, S. Xie, X. Wang, C. Wang, Y. Li, T. E. Shaw, L. Ma, S. N. Ehrlich, A. Liu, J. Ji, F. Gao, L. Dong, F. Liu, *Chem. Eng. J.* **2021**, *426*, 131855; b) Z. Fei, Y. Yang, M. Wang, Z. Tao, Q. Liu, X. Chen, M. Cui, Z. Zhang, J. Tang, X. Qiao, *Chem. Eng. J.* **2018**, *353*, 930–939; c) T. Y. Kardash, E. M. Slavinskaya, R. V. Gulyaev, A. V. Zaikovskii, S. A. Novopashin, A. I. Boronin, *Top. Catal.* **2017**, *60*, 898–913.
[10] X. Yao, Y. Xiong, W. Zou, L. Zhang, S. Wu, X. Dong, F. Gao, Y. Deng, C. Tang, Z. Chen, L. Dong, Y. Chen, *Appl. Catal. B* **2014**, *144*, 152–165.
[11] T. Baidya, A. Gupta, P. A. Deshpandey, G. Madras, M. S. Hegde, *J. Phys. Chem. C.* **2009**, *113*, 4059–4068.
[12] T. Y. Kardash, E. A. Derevyannikova, E. M. Slavinskaya, A. I. Stadnichenko, V. A. Maltsev, A. V. Zaikovskii, S. A. Novopashin, A. I. Boronin, K. M. Neyman, *Front. Chem.* **2019**, *7*,■■Please add page numbers■■.
[13] a) X. Zeng, R. Zhang, X. Xu, X. Wang, *J. Rare Earth* **2012**, *30*, 1013–1019; b) P. Chesler, C. Hornoiu, V. Bratan, C. Munteanu, G. Postole, N. I. Ionescu, T. Juzsakova, A. Redey, M. Gartner, *React. Kinet. Mech. Catal.* **2016**, *117*, 551–563.
[14] F. Li, X. Yu, H. Pan, M. Wang, X. Xin, *Solid State Sci.* **2000**, *2*, 767–772.
[15] A. M. Ganzler, M. Casapu, F. Maurer, H. Stormer, D. Gerthsen, G. Ferre, P. Vernaux, B. Bornmann, R. Frahm, V. Murzin, M. Nachtegaal, M. Votsmeier, J. D. Grunwaldt, *ACS Catal.* **2018**, *8*, 4800–4811.
[16] Y. Ou, G. Zhu, P. Liu, Y. Jia, L. Zhu, J. Nie, S. Zhang, W. Zhang, J. Gao, H. Lu, Y. Huang, X. Shi, M. Hojamberdiev, *ACS Sens.* **2022**, *7*, 1201–1212.
[17] C. Schilling, A. Hofmann, C. Hess, M. V. Ganduglia-Pirovano, *J. Phys. Chem. C.* **2017**, *121*, 20834–20849.

[18] S. Ren, W. Liang, Q. Li, Y. Zhu, *Chemosphere* **2020**, *251*, 126382.
[19] Z. Wu, M. Li, D. R. Mullins, S. H. Overbury, *ACS Catal.* **2012**, *2*, 2224–2234.
[20] J. Chen, Y. Wanyan, J. Zeng, H. Fang, Z. Li, Y. Dong, R. Qin, C. Wu, D. Liu, M. Wang, Q. Kuang, Z. Xie, L. Zheng, *ACS Sustainable Chem. Eng.* **2018**, *6*, 14054–14062.
[21] D.-Y. Wei, M.-F. Yue, S.-N. Qin, S. Zhang, Y.-F. Wu, G.-Y. Xu, H. Zhang, Z.-Q. Tian, J.-F. Li, *J. Am. Chem. Soc.* **2021**, *143*, 15635–15643.
[22] Y. M. Choi, H. Abernathy, H.-T. Chen, M. C. Lin, M. Liu, *ChemPhysChem* **2006**, *7*, 1957–1963.
[23] Y. Liu, Y. Cai, X. Tang, C. Shao, Y. You, L. Wang, W. Zhan, Y. Guo, Y. Zhao, Y. Guo, *Appl. Surf. Sci.* **2022**, *605*, 154675.
[24] a) H. Zhang, J. Wang, Y. Zhang, Y. Jiao, C. Ren, M. Gong, Y. Chen, *Appl. Surf. Sci.* **2016**, *377*, 48–55; b) J. Lee, Y. Ryou, X. Chan, T. J. Kim, D. H. Kim, *J. Phys. Chem. C.* **2016**, *120*, 25870–25879.
[25] F. Dvořák, M. Farnesi Camellone, A. Tovt, N.-D. Tran, F. R. Negreiros, M. Vorokhta, T. Skála, I. Matolínová, J. Mysliveček, V. Matolín, S. Fabris, *Nat. Commun.* **2016**, *7*, 10801.
[26] W. Wan, J. Geiger, N. Berdunov, M. Lopez Luna, S. W. Chee, N. Daelman, N. López, S. Shaikhutdinov, B. Roldan Cuenya, *Angew. Chem. Int. Ed.* **2022**, *61*, e202112640.
[27] D. Kunwar, S. Zhou, A. DeLaRiva, E. J. Peterson, H. Xiong, X. I. Pereira-Hernández, S. C. Purdy, R. ter Veen, H. H. Brongersma, J. T. Miller, H. Hashiguchi, L. Kovarik, S. Lin, H. Guo, Y. Wang, A. K. Datye, *ACS Catal.* **2019**, *9*, 3978–3990.
[28] a) H. A. Aleksandrov, K. M. Neyman, K. I. Hadjiivanov, G. N. Vayssilov, *Phys. Chem. Chem. Phys.* **2016**, *18*, 22108–22121; b) P. Bazin, O. Saur, J. C. Lavalley, M. Daturi, G. Blanchard, *Phys. Chem. Chem. Phys.* **2005**, *7*, 187–194.
[29] W. Tan, S. Xie, X. Wang, J. Xu, Y. Yan, K. Ma, Y. Cai, K. Ye, F. Gao, L. Dong, F. Liu, *ACS Catal.* **2022**, *12*, 12643–12657.
[30] a) L. R. Borges, A. G. M. da Silva, A. H. Braga, L. M. Rossi, M. A. Suller Garcia, P. Vidinha, *ChemCatChem* **2021**, *13*, 1340–1354; b) A. I. Boronin, E. M. Slavinskaya, A. Figueroba, A. I. Stadnichenko, T. Y. Kardash, O. A. Stonkus, E. A. Fedorova, V. V. Muravev, V. A. Svetlichnyi, A. Bruix, K. M. Neyman, *Appl. Catal. B* **2021**, *286*, 119931.

Manuscript received: November 4, 2022
Accepted manuscript online: December 25, 2022
Version of record online: ■■, ■■■

RESEARCH ARTICLE

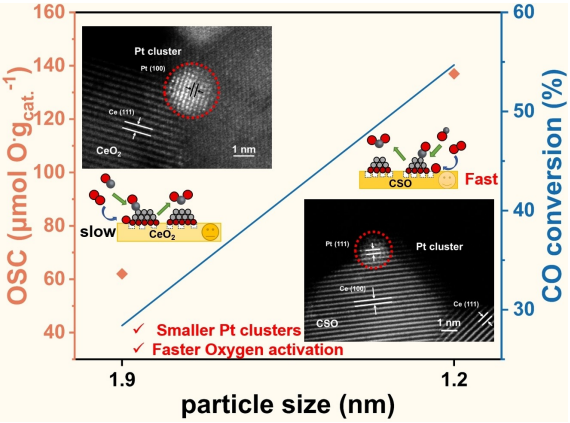

Q. Liu, P. Yang, W. Tan, Y. Haowei, J. Ji, C. Wu, Y. Cai, S. Xie, F. Liu, S. Hong, K. Ma, F. Gao, L. Dong*

1 – 13

Fabricating Robust Pt Clusters on Sn-Doped CeO_2 for CO Oxidation: A Deep Insight into Support Engineering and Surface Structural Evolution

A simple Sn-doped CeO_2 approach was introduced to create oxygen-rich vacancies. Pt/CSO-a exhibited superior CO oxidation performance after reduction activation. Oxygen vacancies limited Pt agglomeration and Pt/CSO-a had a smaller particle size. More exposed active sites enhanced the ability to activate oxygen.■■Ok? Feel free to adjust the ToC paragraph if required. It should contain 40–80 words. Please note that a running text is required for the ToC section, no bullet points please.■■

Fabricating Robust Pt Clusters on Sn-Doped CeO_2 for CO Oxidation: A Deep Insight into Support Engineering and Surface Structural Evolution (Gao et al.)

Share your work on social media! *Chemistry - A European Journal* has added Twitter as a means to promote your article. Twitter is an online microblogging service that enables its users to send and read short messages and media, known as tweets. Please check the pre-written tweet in the galley proofs for accuracy. If you, your team, or institution have a Twitter account, please include its handle @username. Please use hashtags only for the most important keywords, such as #catalysis, #nanoparticles, or #proteindesign. The ToC picture and a link to your article will be added automatically, so the **tweet text must not exceed 250 characters**. This tweet will be posted on the journal's Twitter account (follow us @ChemEurJ) upon publication of your article in its final (possibly unpaginated) form. We recommend you to re-tweet it to alert more researchers about your publication, or to point it out to your institution's social media team.

Please check that the ORCID identifiers listed below are correct. We encourage all authors to provide an ORCID identifier for each coauthor. ORCID is a registry that provides researchers with a unique digital identifier. Some funding agencies recommend or even require the inclusion of ORCID IDs in all published articles, and authors should consult their funding agency guidelines for details. Registration is easy and free; for further information, see http://orcid.org/.

Fei Gao http://orcid.org/0000-0001-8626-5509
Song Hong
Peng Yang
Jiawei Ji http://orcid.org/0000-0003-0199-0491
Qinglong Liu http://orcid.org/0000-0002-5735-485X
Shaohua Xie http://orcid.org/0000-0003-1550-7421
Yandi Cai
Yu Haowei
Cong Wu
Lin Dong
Fudong Liu http://orcid.org/0000-0001-8771-5938
Kaili Ma
Wei Tan http://orcid.org/0000-0002-1481-9346